Peripheral elastic and inelastic scattering of ^{17,18}O on light targets at 12 MeV/nucleon

T. Al-Abdullah[1,3], F. Carstoiu[2]*, C.A. Gagliardi[1], G. Tabacaru[1], L. Trache[1,2] and R.E. Tribble[1]

[1]*Cyclotron Institute, Texas A&M University, College Station, Texas 77843, USA*
[2]*National Institute for Physics and Nuclear Engineering Horia Hulubei, Bucharest, Romania*
[3]*Physics Department, The Hashemite University. Zarqa, Jordan*
(Dated: June 25, 2018)

A study of interaction of neutron rich oxygen isotopes ^{17,18}O with light targets has been undertaken in order to determine the optical potentials needed for the transfer reaction ^{13}C(^{17}O,^{18}O)^{12}C. Optical potentials in both incoming and outgoing channels have been determined in a single experiment. This transfer reaction was used to infer the direct capture rate to the ^{17}F(p,γ)^{18}Ne which is essential to estimate the production of ^{18}F at stellar energies in ONe novae. The success of the asymptotic normalization coefficient (ANC) as indirect method for astrophysics is guaranteed if the reaction mechanism is peripheral and the DWBA cross section calculations are warranted and stable against OMP used. We demonstrate the stability of the ANC method and OMP results using good quality elastic and inelastic scattering data with stable beams before extending the procedures to rare ion beams. The peripherality of our reaction is inferred from a semiclassical decomposition of the total scattering amplitude into barrier and internal barrier components. Comparison between elastic scattering of ^{17}O, ^{18}O and ^{16}O projectiles is made.

PACS numbers: 25.70.Bc, 25.70.Hi, 24.10.Ht.

I. INTRODUCTION

The ^{17}F(p,γ)^{18}Ne reaction is important for understanding nucleosynthesis in novae and plays a role in determining if radioactive nuclei with characteristic gamma-ray signature are produced in sufficient yield to be observed by gamma-ray satellites. The reaction rate is expected to be dominated by direct-capture cross section at nova temperatures and influences the abundances of ^{15}O, ^{17}F, ^{18}F and ^{18}Ne [1]. The rate also determines the ^{17}O/^{18}O ratio that is produced and explains the transition sequence from the HCNO cycle to the *rp*-process [2].

The importance of the direct capture to the bound states in ^{18}Ne has been recently estimated by our team [3]. Because of the difficulties of obtaining information from experiments with radioactive beams, the asymptotic normalization coefficients (ANCs) as an alternative technique to determine this direct capture reaction rate has been used. The spectroscopic factors for the major components of the lowest lying states in mirror nuclei are the same, so the ANC method can be applied to the mirror nucleus ^{18}O and used to extract the ANCs for the g.s., $E_x\left(2_1^+\right) = 1.982$ MeV and $E_x\left(2_2^+\right) = 3.920$ MeV states and convert them to their corresponding states in ^{18}Ne. The primary goal of the experiment was the measurement of the peripheral neutron transfer reaction ^{13}C(^{17}O,^{18}O)^{12}C. Optical potentials in the incoming and outgoing channels have been obtained by measuring elastic scattering angular distributions ^{17}O+ ^{13}C and ^{18}O+ ^{12}C at 12 MeV/nucleon incident energy. The quality of the obtained potentials has been also checked from in-

elastic scattering to selected states in ^{17}O* and ^{18}O*. Since the ANC method assumes the peripherality of the reaction mechanism, we discuss here rather extensively this issue by decomposing semiclassically the total scattering amplitude into barrier and internal barrier subcomponents. We show that the internal barrier subcomponent, which corresponds to the flux penetrating the barrier, gives negligible small contribution to the total cross section, and thus the reaction is peripheral. The elastic scattering ^{17}O+^{13}C includes a fragile target. A difficulty in obtaining the optical model parameters in this type of reactions may arise due to the competition between the increased refractive power of the real potential and increased absorption at the nuclear surface. The well known existence of many ambiguities in the optical model parameters extracted from elastic scattering can raise questions about the reliability and accuracy of these determinations.

Previously, ^{18}O+^{12}C elastic scattering at barrier energies was measured by Robertson *et al.*[4], by Szilner *et al.*[5] and Rudchik *et al.*[6] at some 5-7 MeV/nucleon. Fresnel scattering of ^{18}O on ^{28}Si was measured by Mermaz *et al.*[7] at 56 MeV. For the ^{17}O+ ^{13}C reaction the data are rather scarce, we identified a single fusion study and poor elastic angular distributions at barrier energies [8]. The main conclusion of these studies was that the interaction of ^{17,18}O nuclei with light targets is slightly more absorptive compared with that of the closed shell nucleus ^{16}O and that no significant effects due to the neutron excess were identified.

In Sec. II we give a short description of the experiment. Elastic scattering data and the derivation of the OM potentials are discussed in Sec. III. The semiclassical (WKB) method is used in Sec IV to decompose the total scattering amplitude into barrier and internal barrier components. Inelastic angular distributions to selected

*carstoiu@theory.nipne.ro

states in $^{18}O^*$ and $^{17}O^*$ are discussed in Sec. V. Our conclusions are summarized in Sec. VI.

II.   THE EXPERIMENT

The primary goal of the experiment was the measurement of the transfer reaction $^{13}C(^{17}O,^{18}O)^{12}C$ at 12 MeV/nucleon. In addition, elastic scattering in both incoming and outgoing channels as well as inelastic scattering to selected states in ^{17}O and ^{18}O were measured.

The experiment was carried out with two separate ^{17}O and ^{18}O beams from K500 superconducting cyclotron at Texas A&M University. Each beam was transported through the beam analysis system to the scattering chamber of the multipole-dipole-multipole (MDM) magnetic spectrometer [9], where it interacted with 100 $\mu g/cm^2$ self-supporting targets.

First, the ^{17}O beam impinged on ^{13}C target. The elastic scattering angular distribution was measured for the spectrometer angles 4°-25° in the laboratory system. Fine tuned RAYTRACE [10] calculations were used to reconstruct the position of particles in the focal plane and the scattering angle at the target. A $4° \times 1°$ wide-opening mask and an angle mask consisting of five narrow ($\Delta\theta = 0.1°$) slits were used for each spectrometer angle to double-check the absolute values of the cross section and the quality of the angle calibration. The instrumental setup, including the focal plane detector, and processes for energy and angle calibrations, are identical to that described in Ref. [11]. Second, the ^{12}C target was bombarded by ^{18}O beam with 216 MeV total laboratory energy. The elastic scattering cross section was measured at 4°-22° spectrometer angles.

The angular resolution, $\Delta\theta_{res}$, of the detector in both cases was on average 0.31° in c.m. frame and the position resolution was better than 1 mm. The low lying spectrum of ^{18}O as a function of the position in the focal plane is shown in Fig.1. The spectrum is taken at the spectrometer angle of 4°. The peaks corresponding to elastic scattering and to inelastic transitions to the 2_1^+ and 2_2^+ excited states were observed with sufficient statistics over the whole angular range to obtain good angular distributions. Small amounts of heavy impurities in the target most likely Ta and Si dominate the spectrum at small angles (bellow $\theta_{lab} = 3°$). The absolute values of the cross section were determined by a careful integration of beam charge in a Faraday cup and the measurement of target thickness from the energy loss using alpha particles from sources and the beam. The overall normalization of data was also extensively checked by comparing the data at the most forward angles with optical model calculation. At these angles the cross section is less sensitive to the nuclear potential. The main uncertainties in the data are due to 7.5% in the target thickness and 3% statistical errors. The average normalization error was less than 3%.
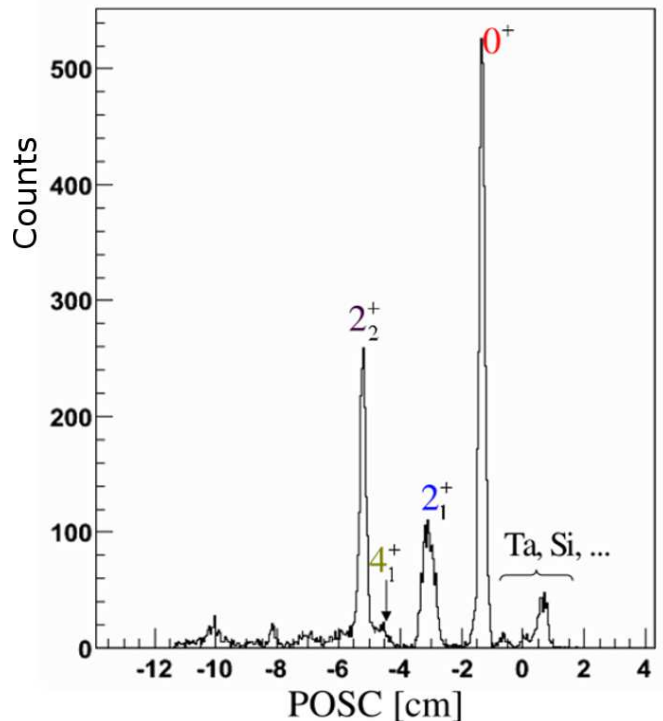

FIG. 1: (Color online) Low-lying spectrum of ^{18}O versus the particle position in the focal plane, measured at the spectrometer angle of 4°. The peaks at the right of the elastic peak are due to Si and Ta contaminants in the target holder.

III.   ELASTIC SCATTERING

A.   Woods-Saxon formfactors

The measured elastic scattering data at E_{lab}=216 and 204 MeV are shown in Figs. 2 and 3. The data are first analyzed using optical potentials with conventional Woods-Saxon (WS) form factors for the nuclear term, supplemented with a Coulomb potential generated by a uniform charge distribution with a reduced radius fixed to r_c=1 fm. No preference has been found for volume or surface localized absorption and throughout the paper only volume absorption is considered. In the absence of any spin dependent observables, spin-orbit or tensor interactions have been ignored. Ground state reorientation couplings have been neglected also. The potential is defined by six parameters specifying the depth and geometry of the real and imaginary terms, with the standard notations, the same as used in Ref. [12]. The number of data points N is quite large, and consequently the usual goodness of fit criteria (χ^2) normalized to N has been used.

Using the strength of the real component of the optical potential as a control parameter, a grid search procedure revealed a number of discrete solutions. Their parameters are presented in Table I. All of the potentials give relatively small χ^2, but only those with the smallest values for entrance and exit channels, potential

pot	V MeV	W MeV	r_V fm	r_W fm	a_V fm	a_W fm	χ^2	σ_R mb	J_V MeV fm³	R_V fm	J_W MeV fm³	R_W fm
							^{18}O+^{12}C at 216 MeV					
PP5	89.18	25.24	0.88	1.16	0.88	0.68	5.12	1712	197	4.69	103	5.09
PP6	195.40	25.59	0.68	1.16	0.96	0.67	6.39	1702	257	4.40	104	5.07
PP7	295.82	26.00	0.60	1.16	0.95	0.67	7.54	1696	297	4.20	106	5.06
PP8	374.41	26.19	0.58	1.16	0.90	0.68	9.78	1695	334	4.01	107	5.06
PP9	75.68	26.16	0.89	1.15	0.93	0.66	5.31	1677	178	4.85	104	5.02
							^{17}O+^{13}C at 204 MeV					
T1	94.69	26.91	.91	1.13	.84	.67	4.47	1659	215	4.67	99	4.96
T2	188.40	24.95	.72	1.12	.94	.69	4.62	1667	271	4.44	92	4.99
T3	248.75	26.36	.69	1.13	.90	.66	4.53	1659	318	4.27	99	4.97
T4	275.49	25.63	.73	1.15	.81	.65	5.90	1660	365	4.11	100	5.00

TABLE I: Discrete solutions obtained with WS form factors for ^{18}O+^{12}C at 216 MeV and ^{17}O+^{13}C at 204 MeV. The line labeled PP9 is a WS phase equivalent of the JLM1 solution.

pot	N_V	N_W	t_V	t_W	χ^2	σ_R mb	J_V MeV fm³	R_V fm	J_W MeV fm³	R_W fm
						^{18}O+^{12}C at 216 MeV				
M3YZR	0.37	0.20	0.88	0.80	10.72	1812	163	4.60	86	5.06
M3YFR	0.33	0.21	0.88	0.86	8.15	1737	164	4.68	103	4.83
GOGNY1	0.28	0.18	0.89	0.87	7.27	1707	158	4.70	103	4.83
GOGNY3	0.37	0.21	0.91	0.84	7.39	1767	158	4.69	89	5.08
JLM1	0.33	0.93	0.87	0.86	6.87	1675	178	4.55	109	4.80
JLM3	0.36	1.02	0.86	0.85	6.75	1708	180	4.56	102	4.85
						^{17}O+^{13}C at 204 MeV				
M3YZR	0.46	0.22	0.91	0.85	5.24	1742	203	4.48	95	4.80
M3YFR	0.38	0.18	0.93	0.86	5.16	1738	196	4.52	94	4.87
GOGNY1	0.32	0.15	0.94	0.85	5.74	1748	188	4.53	88	4.99
GOGNY3	0.41	0.20	0.95	0.87	6.03	1729	186	4.53	88	4.97
JLM1	0.35	0.72	0.89	0.84	6.06	1691	196	4.47	84	4.96
JLM3	0.37	0.80	0.88	0.83	5.63	1719	192	4.49	81	5.00

TABLE II: Unique solutions obtained with folding form factors for ^{18}O+^{12}C at 216 MeV and ^{17}O+^{13}C at 204 MeV.

T1 and PP5 respectively, were adopted in the DWBA calculations of the neutron transfer reaction [3], while the others were used to determine the uncertainty in the choice of the OMP in either channel. The ambiguity in the optical potential has two main sources: the limited range of the measured angles and the strong absorption. When the strong absorption dominates the reaction mechanism, then the interaction is sensitive only to the surface and several phase equivalent optical potentials will appear. The patterns shown in Figs 2 and 3 show rapid oscillation at forward angles followed by a smooth fall-off at intermediate angles. Assuming pure Fraunhofer scattering at forward angles , we extract a grazing angular momentum $\ell_g \approx 36$ from the angular spacing $\Delta\theta = \pi/(\ell_g + 1/2)$. The corresponding grazing distance is quite large, $R_g \approx 7$ fm, much larger than the distance of touching configuration. We systematically find diffuse real potentials ($a_V \approx 0.9$ fm). This effect may be tentatively attributable to the neutron excess. We find also quite constant volume integrals and rms radii for the imaginary component. As a consequence the total reac-

tion cross section seems to be a well defined observable. Weighted average values from table I and table II are $\sigma_R = 1713 \pm 35$ mb and $\sigma_R = 1699 \pm 36$ mb for ^{18}O+^{12}C and ^{17}O+^{13}C reactions respectively. The larger the real volume integral the smaller reduced radius r_V is required to match the data and the far-side component becomes more structured. For the largest real volume integral an Airy oscillation forward to a primary rainbow becomes apparent. Usually, the dominance of the far-side component beyond the Fraunhofer crossover is interpreted as a signature of refractive effects due to a strongly attractive real potential and weak absorption. We will show bellow that the strong absorption is still the dominant reaction mechanism.

A comparison with the scattering of the tightly bound nucleus ^{16}O is in order. Experimental data [13] and our calculation for ^{16}O+^{12}C at 11.3 MeV/nucleon are displayed in Fig. 4. We did not find any reasonable WS solution with $J_V < 300$ MeV fm³ and so the solution with the lowest acceptable real volume integral is plotted. Since the potential is strong, the far-side component
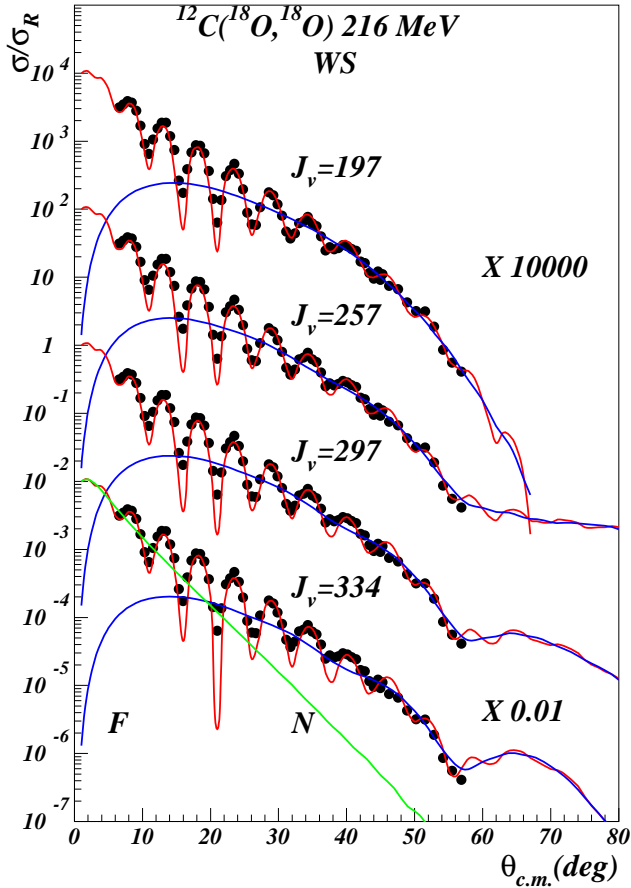
FIG. 2: (Color online) Cross section and far side/near side (F/N) decomposition of the scattering amplitude for WS potentials in Table I. Each calculation is identified by its real volume integral J_V and shifted by factors X to increase the visibility.
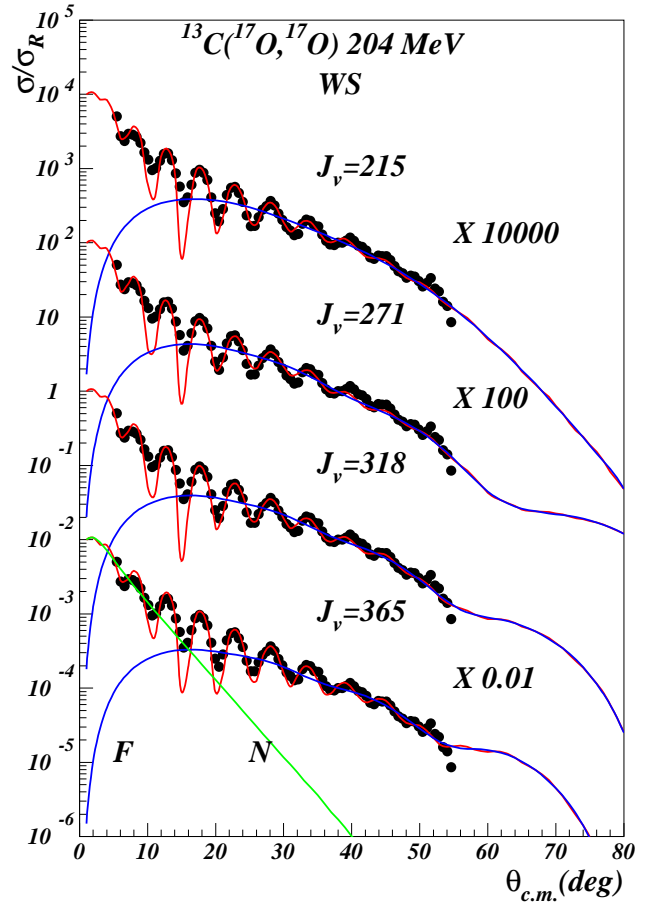
FIG. 3: (Color online) Cross sections and F/N decomposition for the WS potentials Table I. The far side component shows Airy oscillation which moves to forward angles with increased value of the real volume integral.

of the cross section is much more structured. While the Fraunhofer (diffractive) part at forward angles is similar to our reactions, strong refractive effects appear at $\theta > 40°$ as deep Airy oscillations.

B. Folding formfactors

In the following we discuss the ability of the folding model to describe our data. We start by a quite simple model in which the spin-isospin independent formfactor of the OMP is given by the double folding integral,

$$V_{fold}(R) = \int d\vec{r}_1 d\vec{r}_2 \rho_1(r_1)\rho_2(r_2)v_{M3Y}(s) \qquad (1)$$

where v_{M3Y} is the M3Y parametrization of the G-matrix obtained from the Paris NN interaction [14], and $\vec{s} = \vec{r}_1 + \vec{R} - \vec{r}_2$ is the NN separation distance. For the reaction $^{17}O+^{13}C$ we add the small isovector component arising from the nonnegligible neutron skin present in both interacting partners. The Coulomb component of the optical potential is calculated by replacing the nuclear s.p. densities with proton densities and using $v_{coul}(s) = e^2/s$ as effective interaction. The small effect arising from finite proton size is ignored. In the simplest version of this model, dubbed here as M3YZR, the knockon exchange component is simulated by a zero range potential with a slightly energy dependent strength,

$$J_{00}(E) = -276(1 - 0.005E/A) \qquad (2)$$

We keep the number of fitting parameters at the minimum level and take the OMP in the form,

$$U(R) = N_V V(R, t_V) + iN_W V(R, t_W) \qquad (3)$$

where $N_{V,W}$ are normalization constants and $t_{V,W}$ are range parameters defined by the scaling transformation,

$$V(R, t) \to t^3 V_{fold}(tR) \qquad (4)$$

This transformation conserves the volume integral of the folding potential and modifies the radius as,

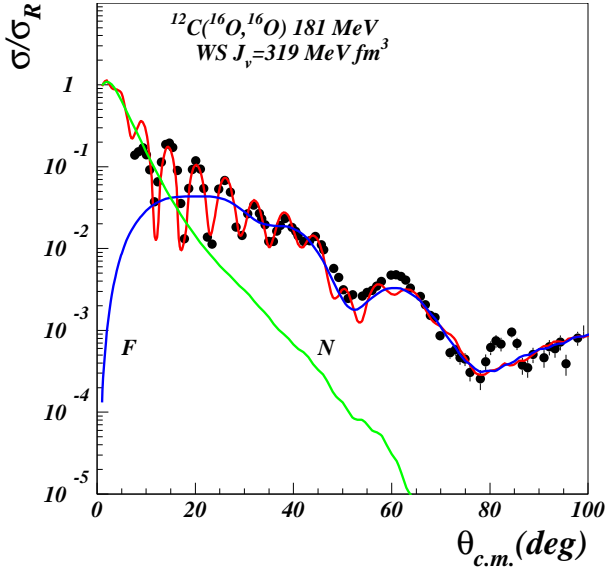FIG. 4: (Color online) Elastic scattering ^{16}O+^{12}C at 11.3 MeV/nucleon. The real part of the WS optical potential is much stronger and the far side component shows several deep Airy oscillations. Experimental data are taken from [13].

Thus the strength of the formfactor is controlled by the parameters $N_{V,W}$. Note that the transformation in Eq. (4) ensures that only the *rms* radius of the bare folding potential is changed. This is in line with the original prescription of [25] which proposed a smearing procedure in terms of a normalized Gaussian function. We found that the transformation in Eq. (4) is more efficient. Based on Eq. (5) one may estimate in an average way the importance of the dynamic polarization potential (DPP) and finite range effects. Throughout this paper we use single particle densities obtained from a spherical Hartree-Fock (HF+BCS) calculation based on the density functional of Beiner and Lombard [15]. The obtained *rms* charge radii are very close to the experimental values [16] and the model predicts a neutron skin $\Delta r = r_n - r_p$ of 0.1, 0.18 and 0.1 fm for ^{13}C, ^{18}O, ^{17}O respectively. The calculated neutron *rms* radii are 2.84 and 2.76 fm for ^{18}O, ^{17}O in good agreement with the values extracted by Khoa *et al.*[17] from high energy interaction cross section. Note that for the fragile ^{13}C ($S_n = 4.9$ MeV) this model predicts a small occupation probability for the neutron $2s_{1/2}$ level of $v^2_{2s_{1/2}} = 0.0016$ but this has a small influence on the tail of the s.p. density. A more elaborate calculation leads to a nonlocal knockon exchange kernel [18],

$$< R^2 >_V = \frac{1}{t^2} < R^2 >_{fold} \qquad (5)$$

$$U_{ex}(\vec{R}^+, \vec{R}^-) = \mu^3 v_{ex}(\mu R^-) \int d\vec{X}_1 \rho_1(X_1) \hat{j}_1(k_{f1}(X_1) \frac{(A_1-1)A_2}{A_1+A_2} R^-) \qquad (6)$$
$$\times \rho_2(|\vec{R}^+ - \vec{X}_1|) \hat{j}_1(k_{f2}(|\vec{R}^+ - \vec{X}_1|) \frac{(A_2-1)A_1}{A_1+A_2} R^-)$$

where $A_{1,2}$ are mass numbers, μ is the reduced mass of the system, $k_{f1,2}$ are Fermi momenta, $R^{+,-}$ are the usual nonlocal coordinates and v_{ex} is the exchange component of the interaction including the long range OPEP tail. Eq. (6) already shows that the nonlocality is small and behaves as $\sim \mu^{-1}$. In the lowest order of the Perey-Saxon approximation, the local equivalent of the nonlocal kernel is obtained by solving the nonlinear equation,

$3j_1(x)/x$ and $j_{0,1}$ are spherical Bessel functions. The local Fermi momenta k_f are evaluated in an extended Thomas-Fermi approximation [19]. We have explored also the extended Slater approximation for the mixed densities of Campi and Bouyssy [20] but did not obtained substantial improvements over the usual Slater approximation. The local momentum for the relative motion is given by,

$$K^2(R) = \frac{2\mu}{\hbar^2} (E_{c.m.} - U_D(R) - U_L(R)) \qquad (8)$$

where U_D is the total direct component of the potential including the Coulomb term. In Eq. (8) we assumed a purely real local momentum of the relative motion since the absorptive component of the OMP is small compared with the real part. The effective mass correction [21], $\frac{\mu^\star}{\mu} = 1 - \frac{\partial U}{\partial E}$ is of the order of a few percent for our systems and is absorbed in the renormalization parameter

$$U_L(R) = 4\pi \int d\vec{r}_1 d\vec{r}_2 \rho_1(r_1) \rho_2(r_2)$$
$$\times \int s^2 ds v_{ex}(s) \hat{j}_1(k_{f1}(r_1)\beta_1 s) \hat{j}_1(k_{f2}(r_1)\beta_2 s)$$
$$\times j_0(\frac{1}{\mu} K(R)s) \delta(\vec{r}_2 - \vec{r}_1 + \vec{R}) \qquad (7)$$

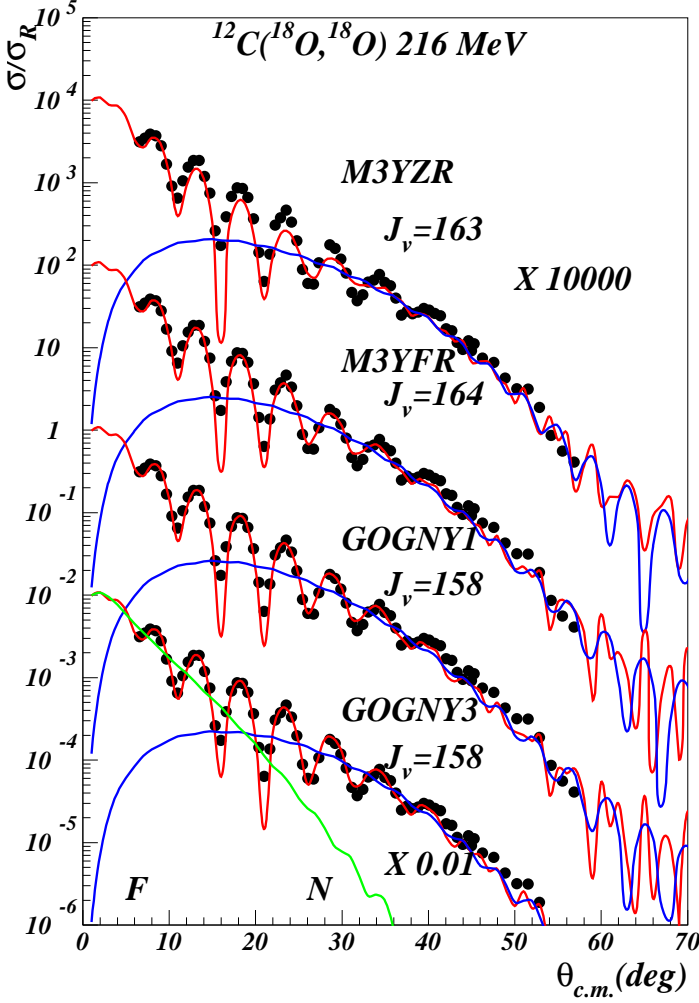Above $\beta_i = (A_i - 1)/A_i$ are recoil corrections, $\hat{j}_1(x) =$

FIG. 5: (Color online) Cross section calculated with folding form factors using the M3Y and GOGNY models. The real volume integral is indicated on each curve. The far side/near side components of the cross section are denoted by F/N. Experimental data and calculation have been shifted by factor X to increase visibility.

FIG. 6: (Color online) The same as in Fig.5 but for the JLM model.

N_W. Some tens of iterations are needed to solve Eq. (7) in order to obtain a precision of 10^{-7} in the entire radial range ($R_{max} = 25$ fm). Calculations with finite range model are dubbed M3YFR.

Neglecting the spin-orbit component, the Gogny NN effective interaction can be expressed as a sum of a central, finite range term and a zero range density dependent term,

$$v(\vec{r}_{12}) = \sum_{i=1}^{2}(W_i + B_iP_\sigma - H_iP_\tau - M_iP_\sigma P_\tau)e^{-\frac{r_{12}^2}{\mu_i^2}} \quad (9)$$

$$+t_3(1 + P_\sigma)\rho^\alpha(\vec{R}_{12})\delta(\vec{r}_{12})$$

where $\vec{r}_{12} = \vec{r}_1 - \vec{r}_2$, $\vec{R}_{12} = (\vec{r}_1 + \vec{r}_2)/2$ and standard notations have been used for parameter strengths and spin-isospin exchange operators. The strengths parameters and the ranges are taken from [22]. The isoscalar
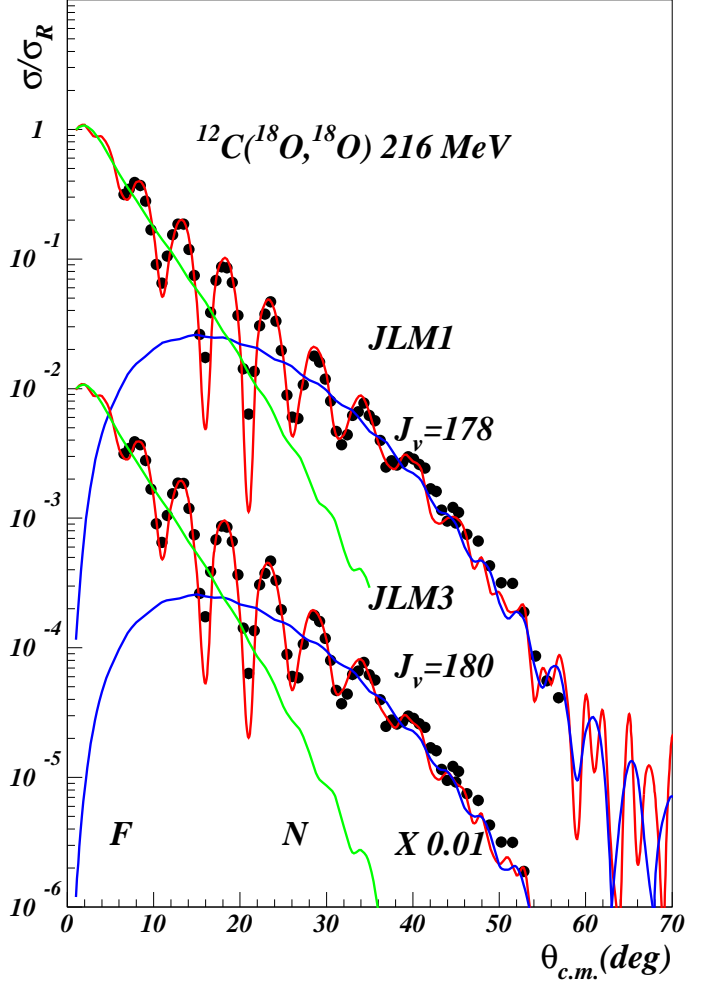
and isovector components of the effective interaction are constructed in the standard way. The interest in this interaction resides in its excellent description (at the HF level) of the saturation properties of the nuclear matter in line with modern estimation from the isoscalar giant monopole [23] or dipole resonance [24] studies. Antisymmetrization of the density dependent term is trivial, so that the sum of direct and exchange term reads,

$$v_D^\rho(r_{12}) + v_{ex}^\rho(r_{12}) = \frac{3t_3}{4}\rho^\alpha\delta(\vec{r}_{12}) \quad (10)$$

The local equivalent of the finite range knockon exchange is calculated with Eq. (7). Two approximations were used for the overlap density,

$$\rho = (\rho_1(r_1)\rho_2(r_2))^{1/2} \quad (11)$$

and

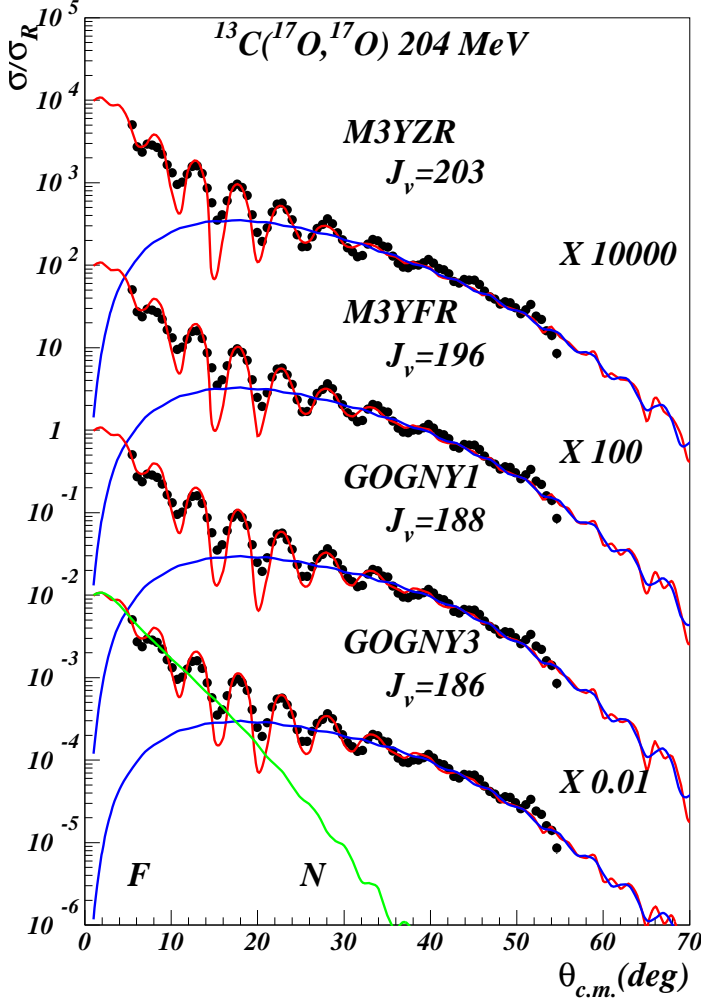$$\rho = \frac{1}{2}(\rho_1(r_1) + \rho_2(r_2)) \quad (12)$$

FIG. 7: (Color online) Cross section and F/N decomposition with folding form factors. Parameters are taken from Table II.

FIG. 8: (Color online) Cross section and F/N decomposition using the JLM form factors.

The first approximation Eq.(11) has the merit that the overlap density goes to zero when one of the interacting nucleons is far from the bulk. In Eq. 12 a factor 1/2 was introduced such as the overlap density does not exceeds the equilibrium density for normal nuclear matter. At large density overlaps, the fusion and other inelastic processes are dominant and the elastic scattering amplitude is negligible small. The calculated OM potentials are dubbed GOGNY1 and GOGNY3 respectively. Both definitions represent crude approximations of the overlap density but are widely used in the estimation of the density dependence effects in the folding model.

We further examine the density dependence effects by using the nuclear matter approach of Jeukenne, Lejeune and Mahaux (JLM) [25] which incorporates a complex, energy and density dependent parametrization of the NN effective interaction obtained in a Brueckner Hartree-Fock approximation from the Reid soft core NN potential. The systematic study [12] of the elastic scattering between p-shell nuclei at energies around 10
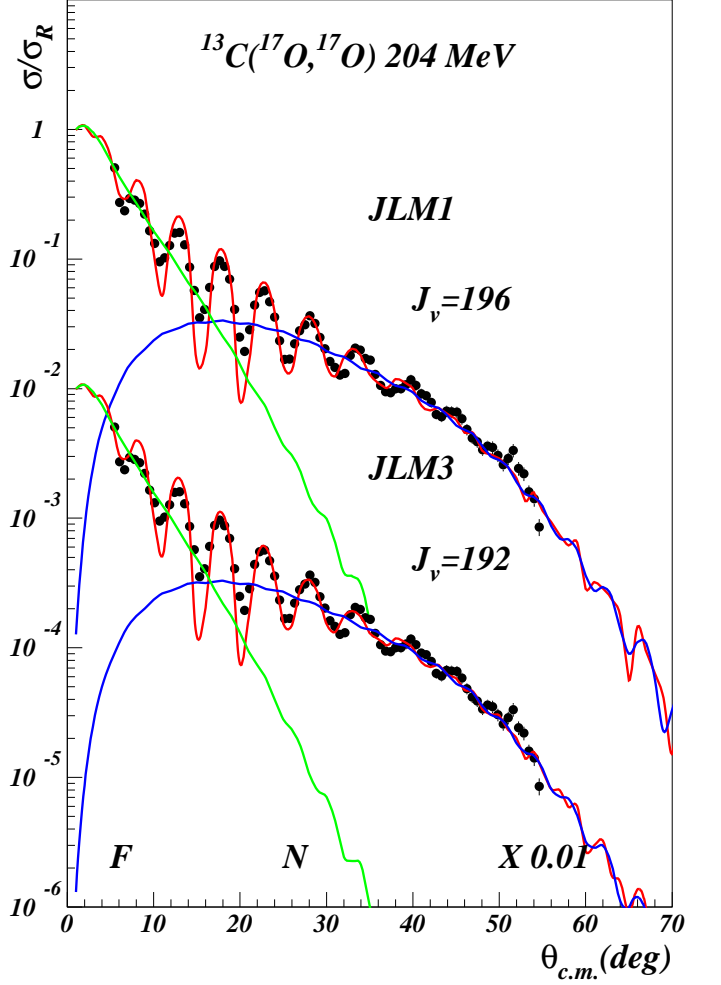
MeV/nucleon leads to the surprising result that on average, the imaginary part of the folded JLM potential was perfectly adequate to describe such reactions and did not need any renormalization ($N_W = 1.00 \pm 0.09$), while the real component needed a substantial renormalization, in line with other effective interactions used in folding models. We examine here to which extent this feature is conserved for tightly bound nuclei in the d shell in the presence of a small neutron excess. Exchange effects are included in this model at the level of N-target interaction. Calculations with this model are dubbed JLM1 and JLM3, depending on which definition we use for the overlap density (eqs.(11) and (12) respectively).

A grid search on the real volume integral reveals a unique solution for all six versions of thee effective interaction, see Table II and Figs 5, 6, 7 and 8. The folding model validates only the solution with the lowest real volume integral found with the WS parametrization. Averaging over all six folding calculations, we find $J_V = 167 \pm 9$ MeV fm^3 for ^{18}O and $J_V = 194 \pm 5$ MeV
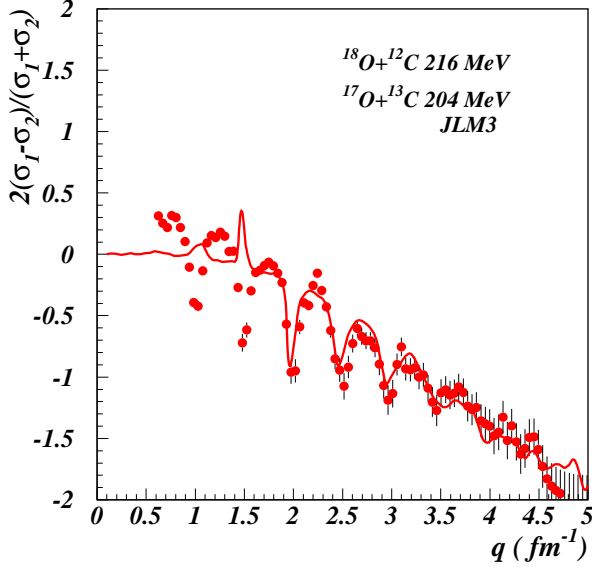
FIG. 9: (Color online) Relative cross section for the elastic scattering $^{18}O+^{12}C$ and $^{17}O+^{13}C$ reactions as a function of momentum transfer is compared with the JLM3 model.

FIG. 11: (Color online) Complex turning points for the WS potential equivalent to JLM1. The stars denote the complex poles of the potential.
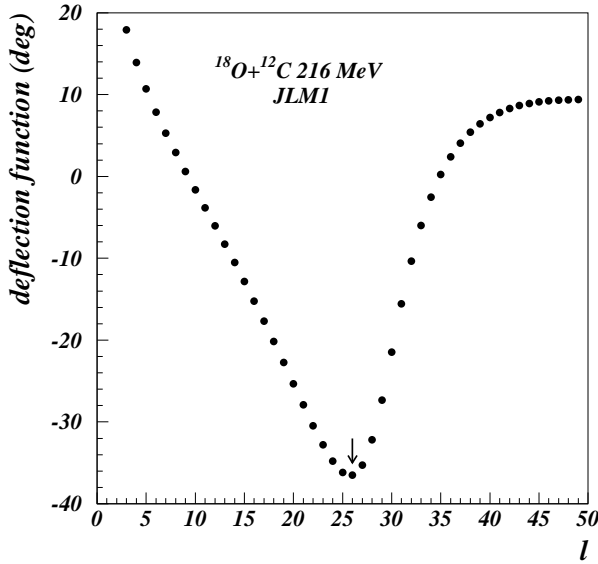

FIG. 10: Classical deflection function for the WS potential equivalent to JLM1. The rainbow angle is $\theta_R = 36°$. The entire measured angular range is illuminated.

FIG. 12: (Color online) Semiclassical absorption profile for the WS potential equivalent to JLM1. The barrier and internal barrier components of the S-matrix are shown by open squares and triangles respectively. The barrier component is typical for strong absorption. The black dots denote the exact quantum result for the same potential and the line is a spline interpolation of the WKB S-matrix.

fm^3 for ^{17}O and so the interaction of ^{17}O is slightly more refractive. Again imaginary volume integrals are quite small pointing to a some transparency of the potential. Correction due to the finite range effects are quite large, of the order of $\Delta R \approx 0.5$ fm for the real potential and much larger for the imaginary potential. The folding calculation reproduces perfectly the diffractive pattern at forward angles and the Fraunhofer F/N crossover produces always an interference maximum. Beyond the cross-over the far-side component decays quite
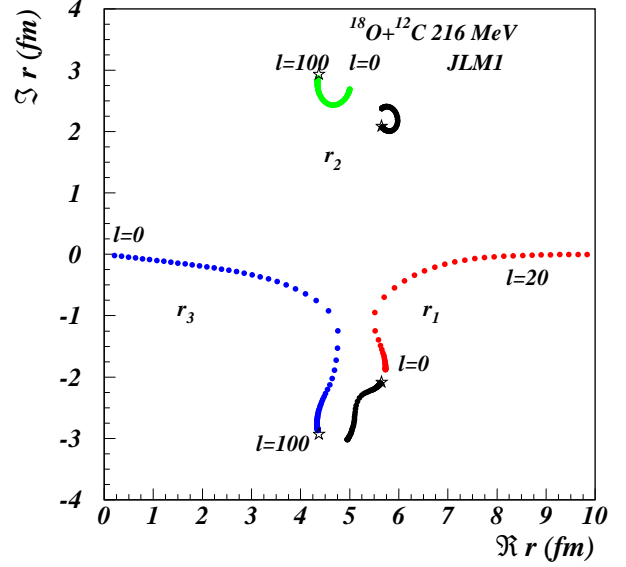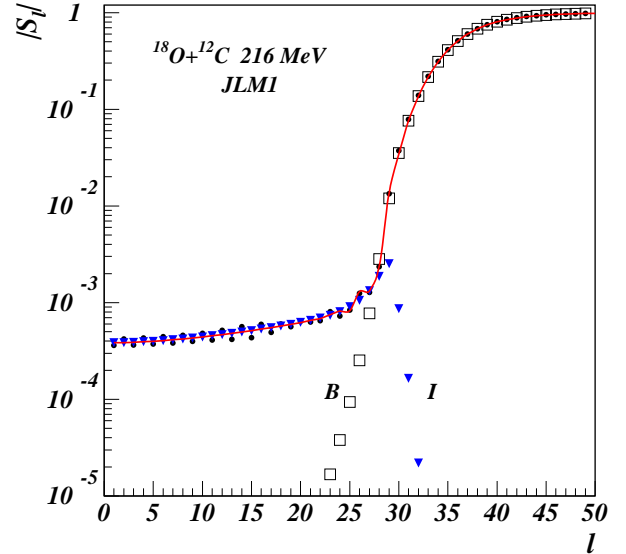
smoothly and shows some glory effects at $\theta > 60°$.

More information one can extract from Fig. 9 where we plot the spectral gradient (or relative cross section) [26],

$$E(q) = 2[\sigma_1(q) - \sigma_2(q)]/[\sigma_1(q) + \sigma_2(q)] \qquad (13)$$
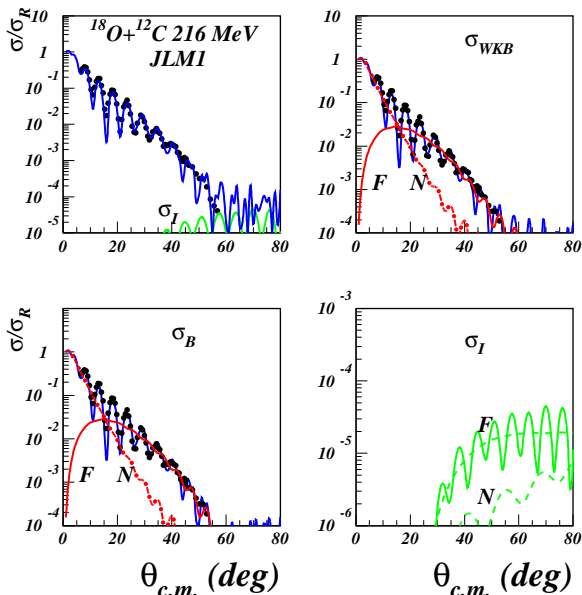
FIG. 13: (Color online) Semiclassical calculation of the cross section based on the WS potential equivalent to JLM1. The WKB scattering amplitude is further decomposed into barrier (σ_B) and internal barrier (σ_I) components. The internal barrier component is negligible small in the measured angular range. The reaction is peripheral.
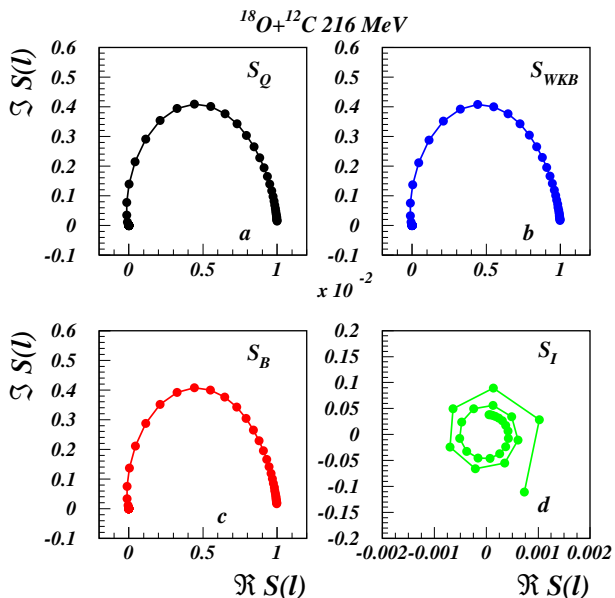

FIG. 14: (Color online) Argand diagram for the semiclassical S-matrix based on the WS potential equivalent to JLM1. The barrier trajectory (panel c) is identical to the exact quantum result (panel a). The small internal barrier component (panel d) shows a hint of an orbiting effect or the presence of Regge poles, but these are too far from the real axis to have noticeable effect in the total cross section.

where σ_1 and σ_2 denote the differential cross sections for ^{18}O and ^{17}O and q is the momentum transfer. The calculation is done with the JLM3 model, since the Glauber

model is questionable at this low energy. The pattern in Fig. 9 confirms the diffractive character of our reactions and an intricate interference effect arising from the variation in the radius of optical model potential and its surface thickness. The disagreement at low momentum transfer arises mostly from the lack of long-range correlation in the HF+BCS model for open shell nuclei. At this point we want to make a comment on the role of the dynamic polarization potential for nuclei with neutron excess over the closed shell. A close examination of the results in Table II shows that we have obtained consistent results for all effective interactions used in the folding model. Our results confirm the conjecture that one can extract from the elastic scattering at best only the low momenta of the interaction (volume integrals and *rms* radii). Corrections in the range parameters are large especially for the imaginary component of the optical potential. We found substantial renormalization for the real part of the optical potential, on average $N_V = 0.36 \pm 0.05$ in line with the previous study [12]. This can be easily understood: the bare folding formfactor has a volume integral around $J_V \approx 450$ MeV fm^3, while the data requires precise values around 160-190 MeV fm^3. Noteworthy, the renormalization of the imaginary component in the JLM model is again quite close to unity. Although the density dependence in the GOGNY and JLM effective interactions is very different, one cannot disentangle between the two models for the overlap density based on the present data, since both of them give identical results.

IV. SEMICLASSICAL BARRIER AND INTERNAL BARRIER AMPLITUDES

Once we have established the main features of the average OM potential, we turn now to study the reaction mechanism using semiclassical methods.

The semiclassical uniform approximation for the scattering amplitude of Brink and Takigawa [27] is well adapted to describe situations in which the scattering is controlled by at most three active, isolated, complex turning points. An approximate multireflection series expansion of the scattering function can be obtained, the terms of which have the same simple physical meaning as in the exact Debye expansion for the scattering of light on a spherical well. The major interest in this theory comes from the fact that it can give precious information on the response of a nuclear system to the nuclear interior.

We take as an example the potential PP9 in Table I which is a WS phase equivalent to the JLM1 optical potential. We discard the absorptive term and define the effective potential as,

$$V_{eff}(r) = V(r) + \frac{\hbar^2}{2\mu}\frac{\lambda^2}{r^2}, \quad \lambda = \ell + \frac{1}{2} \qquad (14)$$

where the Langer prescription has been used for the centrifugal term. This guarantees the correct behavior of
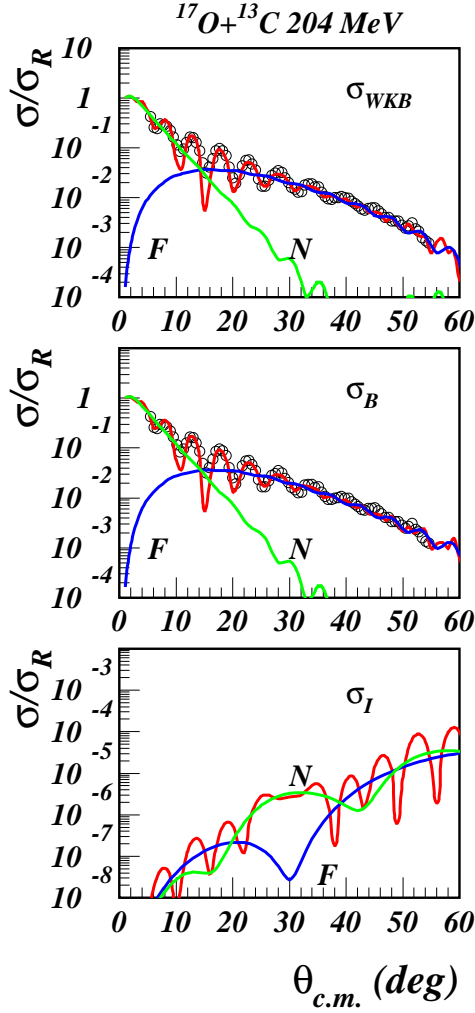
FIG. 15: Semiclassical (WKB) calculation of the cross section based on the T1 potential Table I. The barrier component match perfectly the data in the entire angular range, while the internal barrier component is negligibly small.

the semiclassical wave function at the origin. Then we calculate the deflection function,

$$\Theta(\lambda) = \pi - 2 \int_{r_1}^{\infty} \frac{\sqrt{\frac{\hbar^2}{2\mu}}\lambda \, dr}{r^2 \sqrt{E_{c.m.} - V_{eff}}} \qquad (15)$$

where r_1 is the outer zero of the square root, i.e. the radius of closest approach to the scatterer and μ is the reduced mass. Note that with the replacement $\hbar\lambda = b\sqrt{2\mu E}$, Eq. 15 becomes identical with the classical deflection function $\Theta(b)$, where b is the impact parameter. The result is shown in Fig. 10. The behavior of $\Theta(\lambda)$ is the one expected for an attractive nuclear potential. The nuclear rainbow angle is $\theta_R \approx 36°$. All the measured angular range is classically illuminated and only a few points were measured in the dark side. This explains partially the ambiguities found with the WS formfactors.
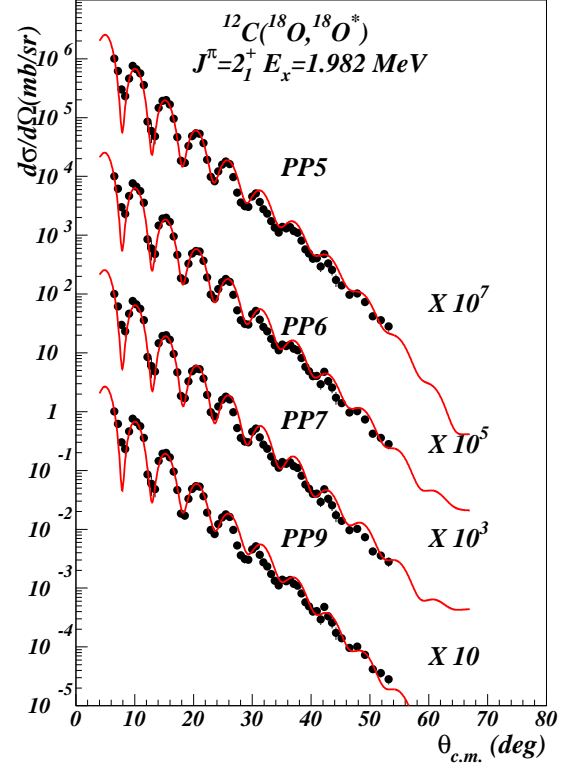

FIG. 16: (Color online) Inelastic cross section to 2_1^+ (1.982 MeV) state in ^{18}O. The DWBA calculation is based on the potentials in Table I.

However this simple calculation does not provide too much information about the interference effects of the corresponding semiclassical trajectories. Going into the complex r-plane we search for complex turning points, i.e. the complex roots of the quantity $E_{c.m.} - V_{eff} - iW$. This is an intricate numerical problem, because, for a WS optical potential, the turning points are located near the potential singularities and there are an infinite number of such poles. The situation for integer angular momenta is depicted in Fig. 11. Active turning points are located near the poles of the real formfactor. Inactive turning points are located quite far from the real axis and give negligible small contribution to the total S-matrix. We observe an ideal situation with three, well isolated, turning points for each partial wave. The multireflection expansion of the scattering function in the Brink-Takigawa approach reads,

$$S_{WKB}(\ell) = \sum_{q=0}^{\infty} S_q(\ell) \qquad (16)$$

where,

$$S_0(\ell) = \frac{\exp(2i\delta_1^{\ell})}{N(S_{21}/\pi)} \qquad (17)$$

and for $q \neq 0$,

$$S_q(\ell) = (-)^{q+1} \frac{\exp\left[2i(qS_{32} + S_{21} + \delta_1^\ell)\right]}{N^{q+1}(S_{21}/\pi)} \quad (18)$$

In these equations δ_1^ℓ is the WKB (complex) phase shift corresponding to the turning point r_1, $N(z)$ is the barrier penetrability factor,

$$N(z) = \frac{\sqrt{2\pi}}{\Gamma(z + \frac{1}{2})} \exp\left(z \ln z - z\right) \quad (19)$$

and S_{ij} is the action integral calculated between turning points r_i and r_j,

$$S_{ij} = \int_{r_i}^{r_j} dr \{ \frac{2\mu}{\hbar^2} [E_{c.m.} - V_{eff} - iW] \}^{1/2} \quad (20)$$
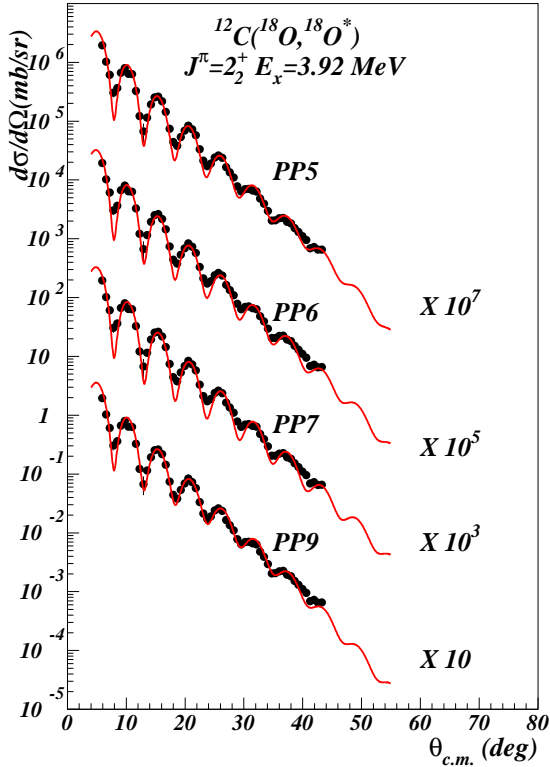

FIG. 17: (Color online) Inelastic cross section to 2_2^+ (3.92 MeV) state in ^{18}O. The DWBA calculation is based on the potentials in Table I.

S_{21} and S_{32} are independent of the integration path provided they lie on the first Riemann sheet and collision with potential poles is avoided. Each term in Eq. 16 has a simple physical interpretation. The first term (the barrier term, denoted also S_B) retains contributions from trajectories reflected at the barrier, not penetrating the internal region. The qth term corresponds to trajectories refracted q times in the nuclear interior with q-1

reflections at the barrier turning point r_2. Summation of terms $q \geq 1$ can be recast into a single term,

$$S_I = \frac{exp[2i(S_{32} + S_{21} + \delta_1^\ell)]}{N(S_{21}/\pi)^2} \frac{1}{1 + \exp\left[2iS_{32}\right]/N(S_{21}/\pi)} \quad (21)$$

and is known as the internal barrier scattering function. The last factor in Eq. 21, the enhancement factor, is responsible for the multiple reflections of the wave within the potential pocket. When the absorption in the nuclear interior is large, the enhancement factor reduces to unity. Since the semiclassical scattering function is decomposed additively, $S_{WKB} = S_B + S_I$, the corresponding total scattering amplitude is decomposed likewise as $f_{WKB} = f_B + f_I$ and conveniently the corresponding barrier and internal barrier angular distributions are calculated as $\sigma_{B,I} = |f_{B,I}|^2$, using the usual angular momentum expansion of the amplitudes.

The poles of the semiclassical S-matrix are given by,

$$N(i\epsilon) + e^{2iS_{32}} = 0 \quad ; \quad \epsilon = -\frac{i}{\pi}S_{21} \quad (22)$$

Semiclassical Regge poles of Eq. 22 are too far from the real axis to have a noticeable influence on the total cross section. The accuracy of the semiclassical calculation has been checked by comparing the barrier and internal barrier absorption profiles with the exact quantum-mechanical result in Fig. 12. One observes that the semiclassical B/I expansion is an *exact* decomposition of the quantum result. They are virtually identical at the scale of the figure. The internal component gets significant values up to the grazing angular momentum (ℓ_g=36) and is negligible small beyond this value. The barrier component resembles a strong absorption profile and this justifies the interpretation that it corresponds to that part of the flux not penetrating into the nuclear interior. Second, the B/I components are almost decoupled in the angular momentum space and therefore they will contribute in different angular ranges.

Semiclassical cross sections are compared with the data in Fig. 13. Better insight into this technique is obtained by further decomposing the B/I components into far and near (BF/BN and IF/IN) subcomponents. Clearly, the barrier component dominates the entire measured angular range. Fraunhofer diffractive oscillations appear as the result of BF and BN interference. At large angles, the internal contribution is negligible and the reaction is peripheral.

The Argand diagrams corresponding to the B/I decomposition is displayed in Fig. 14. The barrier amplitude (panel c) is almost identical with the exact quantum result (panel a) while the internal barrier component shows a nice orbiting effect, but the corresponding dynamical content ($S_I(\ell)$ is too small to have any sizeable effect in the total cross section.

A similar analysis was performed for the reaction ^{17}O+^{13}C based on the WS potential, parameter set T1 Table I. Again we find that the WKB cross section is identical with the exact quantum result based on the same
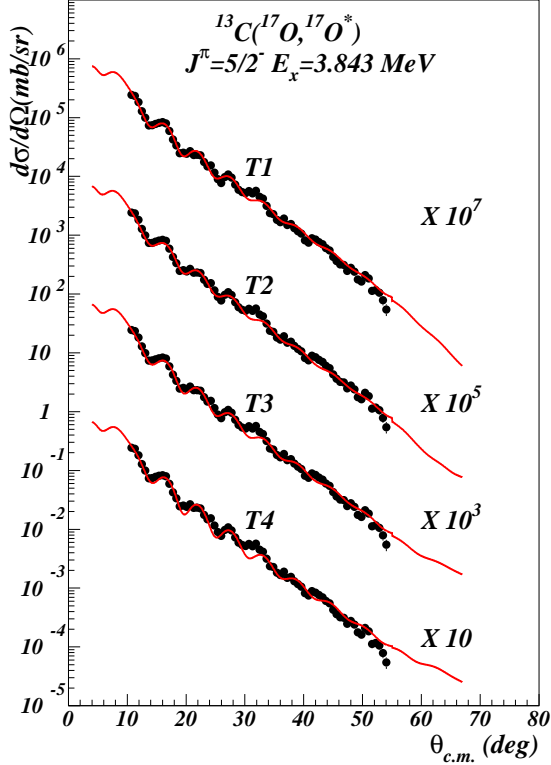
FIG. 18: (Color online) Inelastic cross section to $5/2^-$ (3.84 MeV) state in ^{17}O. The DWBA calculation is based on the potentials in Table I.

FIG. 19: (Color online) Inelastic cross section to $1/2^+$ (6.36 MeV) state in ^{17}O. The DWBA calculation is based on the potentials in Table I.

potential. The barrier component match perfectly the data in the entire angular range, while the internal barrier component gives negligible contribution, see Fig.15. Thus the peripherality character of our reactions is completely demonstrated.

V. INELASTIC TRANSITIONS

We examine in this section the ability of our optical potentials to describe the measured data for inelastic transitions to selected states in ^{18}O ($J^\pi = 2_1^+$, $E_x = 1.982$ MeV, Fig. 16 and $J^\pi = 2_2^+$, $E_x = 3.92$ MeV, Fig. 17) and two transitions in ^{17}O ($J^\pi = \frac{5}{2}^-$, $E_x = 3.843$ MeV, Fig. 18 and $J^\pi = \frac{1}{2}^+$, $E_x = 6.36$ MeV, Fig. 19).

The pattern of our data shows a clear diffractive character since they obey fairly well to the Blair phase rule [28] and therefore a standard DWBA should be an appropriate approach. The deformation table [29] indicates a quadrupole deformation $\beta_2 = 0.107$ for ^{18}O. Other systematics [30] suggests puzzling results with quadrupole deformation ranging from 0.085 up to 0.339. Since the DWBA cross section scales with β_2^2, we execute two calculations using $\beta_2 = 0.015$ and 0.35, chosen rather arbitrary in the range of suggested values. DWUCK4 and
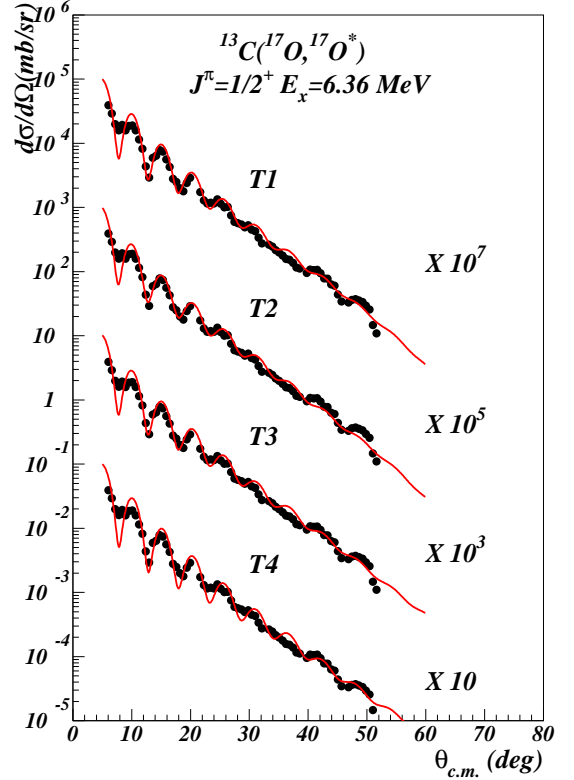
FRESCO give identical shapes for these two values. We then scale the calculation to match the data. The scaled calculations are shown in Fig. 16 and Fig. 17.

The shape of the calculated cross section is virtually identical for all the potentials at the scale of the figure. This proves once again that our potentials are almost phase equivalent, small differences appearing only at large angles much beyond the measured angular range. Remarkably, the calculation with the PP9 parameter set, which is a WS potential phase equivalent to JLM1 folding potential describes the data as well as the other parameter sets. The situation is similar for the other folding potentials. Thus we have obtained a consistent description of both elastic and inelastic cross section using a large palette of optical potentials.

The pattern of the measured transitions in ^{17}O is quite different. The cross section has no forward maximum and decays almost exponentially at large angles with small amplitude wiggles. The experimental study by Cunsolo *et al.*[31] using three particle transfer reaction showed that the low-lying negative parity state in ^{17}O, $J^\pi = \frac{5}{2}^-$, $Ex = 3.843$ MeV is a member of ^{16}O K^+ α-rotational band coupled to $p_{1/2}$ neutron, and thus has a pure $4p-3h$ configuration. The state $J^\pi = \frac{1}{2}^+$, $E_x = 6.36$ MeV, located only 3 keV bellow the α threshold in ^{17}O

is weakly populated in the reaction $^{13}C(^{6}Li,d)^{17}O$ [32]. This state is astrophysically important since it is considered the main source of the $^{13}C(\alpha,n)^{16}O$ reaction rate uncertainty. According to Cunsolo *et al.*[33] this state has a dominant $3p-2h$ structure and belongs to a $(sd)^3$,T=1/2 ^{17}O rotational band. Repeating the procedure used for ^{18}O we obtain a satisfactory description of our data, see Figs. 18 and 19.

VI. CONCLUSIONS

We have measured elastic scattering cross sections for $^{18}O+^{12}C$ and $^{17}O+^{13}C$ at 12 MeV/nucleon as well as inelastic transition to selected states in $^{18}O^*$ and $^{17}O^*$ in order to determine the optical potentials needed to study the one neutron pickup reaction $^{13}C(^{17}O,^{18}O)^{12}C$. Optical potentials in both incoming and outgoing channels were extracted from a standard analysis using Woods-Saxon formfactors. Analysis in terms of semimicroscopic double folding formfactors, using six different approximations for the NN effective interactions helped us to eliminate the ambiguities found with WS potentials. Thus a unique solution emerged from the analysis, which is quite surprising when the reaction mechanism is dominated by strong absorption. We find that the neutron excess over the closed shell leads to a less refractive interaction as compared with the closed shell nucleus ^{16}O. A detailed semiclassical analysis in terms of barrier and internal barrier amplitudes of Brink and Takigawa demonstrated that the flux penetrating the barrier has negligible contribution to the total cross section, and thus the reactions are peripheral. This provides a complete justification for the use of ANC method to extract spectroscopic information from the transfer reaction.

[1] A. Garcia. E. G. Adelberger, P. V. Magnus, D. M. Markoff, K. B. Swartz, M. S. Smith, K. I. Hahn, N. Bateman and P. D. Parker, Phys. Rev. **C43**, 2012 (1991).

[2] R. K. Wallace and S. E. Woosley, Astrophys. J. Suppl. Ser. **45**, 389 (1981).

[3] T. Al-Abdullah, F. Carstoiu, X. Chen, H. L. Clark, C. A. Gagliardi, Y.-W. Lui, A. Mukhamedzhanov, G. Tabacaru, Y. Tokimoto, L. Trache, R. E. Tribble, and Y. Zhai, .Phys. Rev. **C89**, 025809 (2014).

[4] B. C. Robertson, J. T. Sample, D. R. Goosman, K. Nagatani and K. W. Jones, Phys. Rev. **C4**, 2176 (1971).

[5] S. Szilner, M. P. Nicoli, Z. Basrak, R. M. Freeman, F. Haas, A. Morsad, M. E. Brandan, and G. R. Satchler, Phys. Rev. **C64**, 064614 (2001)

[6] A. T. Rudchik et al., Eur. Phys. J.**A44**, 221 (2010).

[7] M. C. Mermaz, M. A. G. Fernandes, A. Greiner, B. T. Kim and N. Lisbona, Phys. Rev. **C19**, 794 (1979).

[8] B. Heusch, C. Beck, J. P. Coffin, P. Engelstein, R. M. Freeman, G. Guillaume, F. Haas, and P. Wagner Phys. Rev. **C26**, 542 (1982).

[9] D. M. Pringle, W. N. Catford, J. S. Winfield, D. G. Lewis, N. A. Jelley, K. W. Allen and J. H. Coupland, Nucl. Instrum. Methods Phys. Res. **A245**, 230 (1986).

[10] S. Kowalski and H. A. Enge, computer code RAYTRACE (unpublished), University of Oxford, England, UK, 1986.

[11] A. M. Mukhamedzhanov, V. Burjan, F. Carstoiu, J. Cejpek, H. L. Clark, C. A. Gagliardi, Y.-W. Lui, V. Kroha, L. Trache, R. E. Tribble, H. M. Xu and and X. G. Zhou, Phys. Rev. **C56**, 1302 (1997).

[12] L. Trache, A. Azhari, H. L. Clark, C. A. Gagliardi, Y.-W. Lui, A. M. Mukhamedzhanov, X. Tang, N. Timofeyuk, R. E. Tribble and F. Carstoiu, Phys. Rev. **C61**, 024612 (2000).

[13] Yu. A. Glukhov, S. A. Goncharov, A. S. Dem'yanova, A. A. Ogloblin, M. V. Rozhkov, V. P. Rudakov, V. Trashka, J. Izv. Ross. Akad. Nauk, Ser. Fiz. **65**, 647 (2001).

[14] N. Anantaraman, H. Toki and G. F. Bertsch, Nucl. Phys. **A398**, 269 (1983).

[15] M. Beiner and R. J. Lombard, Ann. Phys. (N.Y.) **86**, 262 (1974).

[16] I. Angeli, Heavy Ion Physics, **8**, 23 (1998).

[17] Dao T. Khoa, Hoang Sy Than, Tran Hoai Nam, Marcella Grasso, and Nguyen Van Giai Phys. Rev. **C 69**, 044605 (2004).

[18] F. Carstoiu and M. Lassaut, Nucl. Phys. **597**, 269 (1996).

[19] Dao T. Khoa, Phys. Rev. **C63**, 034007 (2001).

[20] X. Campi and A. Bouyssy, Phys. Lett. **73B**, 263 (1978).

[21] J. W. Negele and K. Yazaki, Phys. Rev. Lett .**47**, 71 (1981).

[22] D. Gogny, *Proc. Int. Conf. on Nucl. Physics, Munich 1973, eds J. de Boer and H. J. Mang, Vol. 1, p.48.*

[23] D. H. Youngblood, H. L.Clark and Y.-W. Lui, Phys. Rev. Lett. **82**, 691 (1999).

[24] G. Colo, N. Van Giai, P. F. Bortignon and M. R. Quaglia, Phys. Lett. **B485**, 362 (2000).

[25] J. P. Jeukenne, A. Lejeune and C. Mahaux, Phys. Rev. **C16**, 80 (1977)..

[26] J. P. Auger and R. J. Lombard, Phys. Lett. **90B**, 200 (1980).

[27] D. M. Brink and N. Takigawa, Nucl. Phys. **A279**, 159 (1977).

[28] J. S. Blair, Phys. Rev. **115**, 928 (1959).

[29] P. Moller, J. R. Nix, W. D. Myers and W. J. Swiatecki, At. Data Nucl. Data Tables **59**, 185 (1995).

[30] http://cdfe.sinp.msu.ru

[31] A. Cunsolo, A. Foti, G. Imme, G. Pappalardo, G. Raciti, N. Saunier, Phys. Rev. **C24**, 2127 (1981).

[32] S. Kubono, K. Abe, S. Kato, T.Teranishi, M. Kurokawa, X. Liu, N. Imai, K. Kumagai, P. Strasser, M. H. Tanaka, Y. Fuchi, C. S. Lee, Y. K. Kwon, L. Lee, J. H. Ha and Y. K. Kim, Phys. Rev. Lett. **90**, 062501 (2003).

[33] A. Cunsolo, A. Foti, G.Imme, G. Pappalardo and G. Raciti, Phys. Lett. **124B**, 439 (1983).